

# Chirality-dependent topological states in twisted double bilayer graphene

Minhao He<sup>1†</sup>, Jiaqi Cai<sup>1†</sup>, Ya-Hui Zhang<sup>2</sup>, Yang Liu<sup>1</sup>, Yuhao Li<sup>1</sup>, Takashi Taniguchi<sup>3</sup>, Kenji Watanabe<sup>4</sup>, David H. Cobden<sup>1</sup>, Matthew Yankowitz<sup>1,5#</sup>, and Xiaodong Xu<sup>1,5#</sup>

<sup>1</sup>Department of Physics, University of Washington, Seattle, Washington, 98195, USA

<sup>2</sup>Department of Physics, Harvard University, Cambridge, MA, USA

<sup>3</sup>International Center for Materials Nanoarchitectonics, National Institute for Materials Science, 1-1 Namiki, Tsukuba 305-0044, Japan

<sup>4</sup>Research Center for Functional Materials, National Institute for Materials Science, 1-1 Namiki, Tsukuba 305-0044, Japan

<sup>5</sup>Department of Materials Science and Engineering, University of Washington, Seattle, Washington, 98195, USA

<sup>†</sup> These authors contributed equally to the work.

<sup>#</sup>Correspondence to: [myank@uw.edu](mailto:myank@uw.edu); [xuxd@uw.edu](mailto:xuxd@uw.edu);

**The properties of van der Waals (vdW) crystals and heterostructures depend sensitively on their layer stacking configuration. The twist angle and lattice mismatch between constituent vdW sheets have been shown to be crucial parameters influencing the strongly correlated and topological states of matter in moiré materials<sup>1,2</sup>. Here, we demonstrate a new approach for controlling these emergent states by altering the stacking chirality of the moiré structure. We study twisted double bilayer graphene (tDBG) in an AB-BA stacking configuration (i.e., with the component Bernal bilayers rotated by nearly 60°) and observe topological and symmetry-broken states that are absent in AB-AB stacked tDBG<sup>3–7</sup>. In particular, we observe an anomalous Hall effect (AHE) at filling factor  $\nu = 3$  (i.e., 3 electrons per moiré cell), implying a correlated ground state that spontaneously breaks time-reversal symmetry. In addition, at fractional filling  $\nu = 7/2$ , a robust symmetry-broken Chern insulator (SBCI) state associated with translational symmetry breaking emerges upon applying a magnetic field, concomitant with an AHE at zero field. Our results motivate future experiments in which the stacking chirality is employed as an important new degree of freedom for controlling the strongly correlated and topological phase diagram of other moiré materials.**

Van der Waals (vdW) crystals are stacked atomic layers characterized by strong in-plane atomic bonding and a weak out-of-plane vdW interaction<sup>8</sup>. Materials comprising identical atomic layers can have a diverse set of metastable layer stacking configurations, providing a high degree of tunability in designing vdW heterostructures. Recent advances in moiré materials<sup>1,2</sup>, exemplified by magic-angle twisted bilayer graphene<sup>9–15</sup> (tBLG), greatly expand the landscape of possible vdW heterostructures by utilizing twist angle and lattice mismatch as key factors in the stacking configuration. In  $(M+N)$  twisted multilayer graphene, comprising rotated sheets of  $M$ - and  $N$ -layer chirally stacked graphene, an additional degree of freedom emerges in which the two multilayer graphene sheets can be stacked with either the same or opposite chirality. The band structure and

topology of twisted multilayer graphene are predicted to depend sensitively on the chirality of the stacking<sup>16–20</sup>; however, this has yet to be explored experimentally.

Here, we investigate the role of the stacking chirality in determining the correlated and topological phase diagram of twisted double bilayer graphene (tDBG), consisting of two sheets of Bernal-stacked bilayer graphene. tDBG samples can be constructed either by assembling the two bilayers with the same (AB-AB) or opposite (AB-BA) stacking chirality (Figs. 1a-b, Supplementary Fig. 1). Whereas tDBG samples with AB-AB stacking have been studied extensively over the past few years<sup>3–7,21–26</sup>, our study focuses on a new class of tDBG samples with AB-BA stacking constructed by rotating the two constituent bilayer graphene sheets by a small twist angle away from 60°. We denote the effective twist angle of the AB-BA tDBG by  $\theta' = 60^\circ - \theta$ , where  $\theta$  is the actual twist between the two bilayers. Although the band dispersions for AB-AB and AB-BA are nearly indistinguishable (Fig. 1c), our calculations show a different distribution of the Berry curvature within the moiré Brillouin zone and correspondingly different Chern numbers of the lowest conduction band (Figs. 1d-e and Supplementary Notes 1-2).

We perform electrical transport measurements on six AB-BA tDBG samples in which  $\theta'$  varies from 1.06° to 1.39° (Supplementary Figs. 2-3), and compare them with AB-AB samples over a similar range of twist angles, denoted by  $\theta$ . Figures 1f-g compare measurements of the resistivity,  $\rho_{xx}$ , of AB-AB and AB-BA tDBG samples as a function of carrier density,  $n$ , and displacement field,  $D$ . The filling factor of the moiré minibands,  $\nu$ , is shown on the top axis, where  $\nu = \pm 4$  corresponds to full filling of the lowest moiré conduction and valence bands (see Methods). The samples have similar twist angles of  $\theta = 1.34^\circ$  (device S1) and  $\theta' = 1.39^\circ$  (device O1), respectively. The AB-AB phase diagram has already been detailed extensively elsewhere<sup>3–7</sup>. In short, we observe gaps at  $\nu = 0$  and  $\pm 4$  tuned by  $D$ , a cross-like resistive feature for  $\nu < 0$  reflecting van Hove singularities in the valence bands, and a ‘halo’-like feature surrounding the insulating state at  $\nu = +2$ , marking the emergence of symmetry-broken correlated metallic and insulating states. Measurement of the Hall coefficient,  $R_H = (R_{xy}[B] - R_{xy}[-B])/(2B)$ , further reveal developing symmetry-broken states at  $\nu = +3$  as well. The primary transport features observed in AB-BA are very similar (see also Supplementary Fig. 4), consistent with the nearly identical band dispersions in our calculations.

A detailed comparison, however, of the resistivity reveals subtle differences between the two stacking chiralities. Most importantly, we observe an anomalous Hall effect (AHE) in AB-BA devices, corresponding to a hysteresis in  $\rho_{xy}$  at zero magnetic field,  $B = 0$ , near  $\nu = +3$  under a finite displacement field. In contrast, there are no signatures of the AHE in any of our AB-AB devices nor in those reported previously by other groups<sup>3–7</sup>. Figures 2a-b shows representative data comparing devices S2 (AB-AB) and O1 (AB-BA), in each case plotting  $\rho_{xy}$  as  $B$  is swept back and forth. The amplitude of the AHE is small in device O1, much less than the quantized value of  $h/e^2$  ( $h$  is Planck’s constant and  $e$  is the charge of the electron). Also, there are numerous hysteretic jumps indicating the existence of multiple magnetic domains between the contacts. Nevertheless, similar behavior is seen near  $\nu = +3$  in two other AB-BA devices (Supplementary Fig. 5) with  $\theta'$  ranging between 1.33° and 1.39°, implying that the AHE is a robust feature of this stacking chirality.

There are many potential correlated ground states that could occur in tDBG at  $\nu = +3$ , including states with full spin and valley polarization<sup>15</sup>, intervalley coherent (IVC) states with various order

parameters<sup>27</sup>, density wave states, and others<sup>17</sup>. Although it is difficult to differentiate between these possibilities in transport experiments unambiguously, the AHE implies that spontaneous time-reversal symmetry (TRS) breaking occurs near  $\nu = +3$  in AB-BA whereas TRS is preserved in AB-AB stacking. Although the nature of the correlated states in the AB-AB case at  $\nu = +1$  and  $+3$  has remained mysterious since their discovery<sup>3,16,17,27</sup>, the occurrence of a TRS-broken state at  $\nu = +3$  in AB-BA implies a critical role for the valley Chern number in determining the ground state. This observation should therefore help elucidate the nature of these states.

We additionally observe AHE in AB-BA devices even at some filling factors far away from integers, as illustrated in Fig. 2c for  $\nu = 3.61$ . To examine the doping dependence of the AHE we map the difference in  $\rho_{xy}$  between the two field sweep directions,  $\Delta\rho_{xy} = \rho_{xy}^{B\downarrow} - \rho_{xy}^{B\uparrow}$  (Fig. 2d), here with  $D = -0.42$  V/nm. We observe two distinct pockets of clear AHE, one around  $\nu = +3$  and one around  $\nu = +3.5$ . The behavior at other values of  $D$  is similar (Supplementary Fig. 6). The separation of the two pockets in doping suggests that they are associated with distinct correlated ground states. Correlated states at non-integer filling of a moiré miniband have been observed previously in graphene aligned with hBN at large magnetic field<sup>28,29</sup>, and more recently in twisted monolayer-bilayer graphene<sup>30</sup> (tMBG) and twisted bilayer graphene (tBLG) aligned with hBN<sup>31</sup> at  $B = 0$ . These states may be associated with a spontaneous charge density wave (CDW) formation that expands the effective unit cell, or perhaps with a moiré lattice-driven charge fractionalization of quasiparticles analogous to the fractional quantum Hall effect<sup>31,32</sup>.

To further explore this effect we study the evolution of  $\rho_{xx}$  and  $\rho_{xy}$  for AB-BA device O1 in a large magnetic field (Figs. 3a-b). We observe a variety of gapped states that evolve with a linear trajectory as described by the Streda formula,  $C = (h/e)\partial n/\partial B$ . These states are characterized by strongly suppressed  $\rho_{xx}$  and (nearly) quantized  $\rho_{xy}$ , with linear trajectories captured by the usual equation  $\nu = Cn_\phi + s$ , where  $n_\phi$  is the number of magnetic flux quanta per moiré cell, the integer  $C$  is the Chern number, and the  $s$  is the band filling index, giving the number of electrons per moiré unit cell at  $B = 0$ . Figure 3c shows a schematic denoting the most robust gapped states observed. States with  $C \neq 0$ ,  $s = 0$ , equivalent to integer quantum Hall states, are indicated in purple, while states with  $C \neq 0$  and  $s$  a nonzero integer, or “Chern insulators,” are indicated in orange, red, or blue depending on the value of  $s$ . Topologically trivial ( $C = 0$ ) insulating states are indicated in black.

In addition to a variety of states with integer  $s$ , there is a robust state with  $C = 1$  and  $s = 7/2$ , indicated by the green dashed line, which persists over a relatively wide range of  $D$  (Supplementary Figs. 7-8). For this state  $\rho_{xy}$  is approximately integer-quantized at  $h/e^2$  for  $B$  above  $\sim 6$  T, making charge fractionalization unlikely. Similar states in recent reports on tMBG<sup>30</sup> and tBLG<sup>31,33</sup> were argued to be symmetry-broken Chern insulators (SBCI) resulting from the formation of a charge density wave (CDW) that doubles the area of the unit cell relative to the moiré cell. To explore this possibility, we performed a modified continuum model calculation generalized to include a CDW order (Supplementary Note 3). This model predicts that the lowest moiré conduction band splits into two gapped subbands upon inclusion of the density wave order (Fig. 3d and Supplementary Fig. 9), with a corresponding electron density profile shown in Fig. 3e. After considering remote band mixing, we calculate a valley Chern number of  $C\nu = 1$  for the higher-energy subband. This is consistent with the observation of a  $C = 1$  state with  $s = 7/2$ , which arises when seven of the eight subbands are filled. As with the AHE at  $\nu = +3$ , we observe this SBCI

state in multiple AB-BA devices (O1, O2, O3) at  $T = 2$  K (Supplementary Fig. 10) but not in any of our AB-AB devices (Supplementary Fig. 11) or those reported by other groups<sup>3–6,25</sup>. Its existence appears to be determined solely by the stacking chirality of tDBG, and hence the distinct Berry curvature and valley Chern number of the AB-BA stacking is likely critical for its occurrence.

Finally, we study an AB-BA sample ( $\theta' = 1.38^\circ$ ) which is also closely aligned to the top encapsulating boron nitride (hBN) crystal (device O2). Measurements of the Landau fan diagram at  $D = 0$  V/nm confirm the existence of a second moiré potential arising from a twist angle of  $0.55^\circ$  between the uppermost graphene and hBN (Supplementary Figure 12). This aligned hBN layer breaks the equivalence of the band structure for opposite orientations of  $D$ . As a result, the correlated states depend on the sign of  $D$  (Fig. 4a), unlike in the hBN-misaligned samples. For positive  $D$ , electrons are pushed away from the graphene layer at the aligned hBN interface (Fig. 4b) while for negative  $D$  they are pushed towards it (Fig. 4c). For positive  $D$ , the correlated insulating state at  $\nu = 2$  resembles that in hBN-misaligned samples, while for negative  $D$  the correlated states are more complicated and exhibit new splitting features. The right-most panel of Fig. 4a shows the temperature dependence of  $\rho_{xx}$  as a function of  $D$  at  $\nu = 2$ . For  $D < 0$  the correlated insulating state at  $\nu = 2$  appears weakened, witnessed by the suppression of  $\rho_{xx}$ . Despite this, we still observe a robust  $C=1, s=7/2$  SBCI state upon applying a magnetic field, albeit with a larger onset field than for  $D>0$  (green dashed lines in Figs. 4d-e). These observations underline the robustness of the correlated and topological phases that are determined by stacking chirality of tDBG, as the SBCI state survives even upon weakening the correlation strength.

In conclusion, we have discovered topological and symmetry-broken states in AB-BA twisted double-bilayer which are absent in the AB-AB stacking. This important stacking chirality degree of freedom is absent in both tBLG and tMBG due to the  $C_6$  rotational symmetry of monolayer graphene. Nonetheless, we anticipate it to play a critical role in other  $M+N$  twisted multilayer graphene systems, as well as in a broad class of moiré materials in which each of the constituent vdW components has  $C_3$  rotation symmetry. Our finding therefore opens up new approach to engineering the topology and correlated states in such systems.

## Methods:

### Sample fabrication

tDBG devices were fabricated using a cut-and-stack method. Bilayer graphene is first cut using an AFM lithography technique, and the two pieces are picked up sequentially while setting the twist angle to the desired value close to  $60^\circ$  in between. We use 3-5 nm graphite as both top and bottom gates. Heterostructures of graphite/hBN/tDBG/hBN/graphite are assembled using a standard dry-transfer technique with a PC/PDMS (polycarbonate/polydimethylsiloxane) stamp and transferred onto a Si/SiO<sub>2</sub> wafer. CHF<sub>3</sub>/O<sub>2</sub> etching and O<sub>2</sub> plasma etching followed by electron beam lithography are used to define a Hall bar geometry, and Cr/Au contacts are finally added using electron beam evaporation. The AB-AB tDBG devices used in the current study are the same as those reported in our previous work<sup>7</sup>.

### Transport measurements

Transport measurements above 2 K were conducted in a Quantum Design PPMS system. Transport measurements below 2 K were conducted in a Bluefors dilution refrigerator with low-

temperature low-pass filters. In both cases, measurements are performed with a 1-5 nA a.c. excitation current at either 13.3 Hz or 13.7 Hz. The current and voltage are pre-amplified by DL 1211 and SR560 respectively, and then read out by SR830/SR860 lock-in amplifiers. Gate voltages are supplied by either NI DAQ or Keithley 2450. A global Si gate is sometimes used to reduce contact resistance issue.

The dual-gate device geometry enables independent control of  $D$  and  $n$ . The relationship between the top and bottom gate voltages,  $V_t$ ,  $V_b$ , and  $n$  and  $D$  are given by  $n = (V_t C_t + V_b C_b)/e$  and  $D = (V_t C_t - V_b C_b)/2\epsilon_0$ , where  $C_t$  and  $C_b$  are the top and bottom gate capacitances per unit area and  $\epsilon_0$  is the vacuum permittivity. We note that our definition of displacement field  $D$  follows the convention in the field whereby it has the same units as electric field.

The filling factor  $\nu$  is defined as the number of electrons per moiré unit cell. Full filling of the four-fold spin-valley degenerate flat bands corresponds to 4 electrons (holes) per moiré unit cell,  $\nu = +4$  ( $-4$ ). The twist angle was first determined by measuring the carrier density corresponding to the band insulators at  $\nu = \pm 4$ , following the relationship  $n = 8\theta^2/\sqrt{3}a^2$ , where  $a = 0.246$  nm is the graphene lattice constant. It is further confirmed by fitting the observed quantum Hall states and Chern insulators with the allowed Hofstadter states in the Wannier diagram. Brown-Zak oscillations were also used to verify the twist angle whenever applicable.

### Band structure calculation

The band structure is calculated following the standard Bistritzer-Macdonald continuum model<sup>9</sup>. Details of the model can be found in Supplementary Note. 1.

**Acknowledgments:** This work was mainly supported by NSF MRSEC 1719797. M.H. and M.Y. acknowledge support from the Army Research Office under Grant Number W911NF-20-1-0211. X.X. and M.Y. acknowledge support from the State of Washington funded Clean Energy Institute. This work made use of a dilution refrigerator system which was provided by NSF DMR1725221. Y.H.L. acknowledges the support of the China Scholarship Council. K.W. and T.T. acknowledge support from the Elemental Strategy Initiative conducted by the MEXT, Japan, Grant Number JPMXP0112101001, JSPS KAKENHI Grant Number JP20H00354 and the CREST (JPMJCR15F3), JST.

**Author Contributions:** X.X. and M.Y. conceived and supervised the experiment. M.H. and J. C. fabricated the devices and performed the measurements. Y.Z. performed the calculations. Y. Liu. and Y. Li. contributed to fabrication of AB-AB stacked devices. D.H.C. assisted with measurements in the dilution refrigerator. K.W. and T.T. provided the bulk hBN crystals. M.H., J.C., M.Y., and X.X. analyzed the data and wrote the paper with input from all authors.

**Competing Interests:** The authors declare no competing interests.

**Data Availability:** All data that support the plots within this paper and other findings of this study are available from the corresponding author upon reasonable request. Source data are provided with this paper.

## References:

1. Andrei, E. Y. *et al.* The marvels of moiré materials. *Nat. Rev. Mater.* **6**, 201–206 (2021).
2. Balents, L., Dean, C. R., Efetov, D. K. & Young, A. F. Superconductivity and strong correlations in moiré flat bands. *Nat. Phys.* **16**, 725–733 (2020).
3. Liu, X. *et al.* Tunable spin-polarized correlated states in twisted double bilayer graphene. *Nature* **583**, 221–225 (2020).
4. Cao, Y. *et al.* Tunable correlated states and spin-polarized phases in twisted bilayer–bilayer graphene. *Nature* **583**, 215–220 (2020).
5. Burg, G. W. *et al.* Correlated Insulating States in Twisted Double Bilayer Graphene. *Phys. Rev. Lett.* **123**, 197702 (2019).
6. Shen, C. *et al.* Correlated states in twisted double bilayer graphene. *Nat. Phys.* **16**, 520–525 (2020).
7. He, M. *et al.* Symmetry breaking in twisted double bilayer graphene. *Nat. Phys.* **17**, 26–30 (2021).
8. Geim, A. K. & Grigorieva, I. V. Van der Waals heterostructures. *Nature* **499**, 419–425 (2013).
9. Bistritzer, R. & MacDonald, A. H. Moiré bands in twisted double-layer graphene. *Proc. National. Acad. Sci.* **108**, 12233–12237 (2011).
10. Cao, Y. *et al.* Correlated insulator behaviour at half-filling in magic-angle graphene superlattices. *Nature* **556**, 80–84 (2018).
11. Cao, Y. *et al.* Unconventional superconductivity in magic-angle graphene superlattices. *Nature* **556**, 43–50 (2018).
12. Yankowitz, M. *et al.* Tuning superconductivity in twisted bilayer graphene. *Science* **363**, eaav1910 (2019).
13. Lu, X. *et al.* Superconductors, orbital magnets and correlated states in magic-angle bilayer graphene. *Nature* **574**, 653–657 (2019).
14. Sharpe, A. L. *et al.* Emergent ferromagnetism near three-quarters filling in twisted bilayer graphene. *Science* **365**, 605–608 (2019).
15. Serlin, M. *et al.* Intrinsic quantized anomalous Hall effect in a moiré heterostructure. *Science* **367**, 900–903 (2020).

16. Zhang, Y.-H., Mao, D., Cao, Y., Jarillo-Herrero, P. & Senthil, T. Nearly flat Chern bands in moiré superlattices. *Phys. Rev. B* **99**, 075127 (2019).
17. Lee, J. Y. *et al.* Theory of correlated insulating behaviour and spin-triplet superconductivity in twisted double bilayer graphene. *Nat. Commun.* **10**, 5333 (2019).
18. Liu, J., Ma, Z., Gao, J. & Dai, X. Quantum Valley Hall Effect, Orbital Magnetism, and Anomalous Hall Effect in Twisted Multilayer Graphene Systems. *Phys. Rev. X* **9**, 031021 (2019).
19. Chebrolu, N. R., Chittari, B. L. & Jung, J. Flat bands in twisted double bilayer graphene. *Phys. Rev. B* **99**, 235417 (2019).
20. Koshino, M. Band structure and topological properties of twisted double bilayer graphene. *Phys. Rev. B* **99**, 235406 (2019).
21. Rubio-Verdú, C. *et al.* Universal moiré nematic phase in twisted graphitic systems. *arXiv: 2009.11645* (2020).
22. Liu, X. *et al.* Spectroscopy of a tunable moiré system with a correlated and topological flat band. *Nat. Commun.* **12**, 2732 (2021).
23. Zhang, C. *et al.* Visualizing delocalized correlated electronic states in twisted double bilayer graphene. *Nat. Commun.* **12**, 2516 (2021).
24. Wang, Y. *et al.* Topological Edge Transport in Twisted Double-Bilayer Graphene. *arXiv: 2101.03621* (2021).
25. Burg, G. W. *et al.* Evidence of Emergent Symmetry and Valley Chern Number in Twisted Double-Bilayer Graphene. *arxiv: 2006.14000* (2020).
26. Chu, Y. *et al.* Phonons and Quantum Criticality Revealed by Temperature Linear Resistivity in Twisted Double Bilayer Graphene. *arXiv: 2104.05406* (2021).
27. He, M. *et al.* Competing correlated states and abundant orbital magnetism in twisted monolayer-bilayer graphene. *Nat. Commun.* **12**, 4727 (2021).
28. Wang, L. *et al.* Evidence for a fractional fractal quantum Hall effect in graphene superlattices. *Science* **350**, 1231–1234 (2015).
29. Spanton, E. M. *et al.* Observation of fractional Chern insulators in a van der Waals heterostructure. *Science* **360**, eaan8458 (2018).
30. Polshyn, H. *et al.* Topological charge density waves at half-integer filling of a moiré superlattice. *arXiv: 2104.01178* (2021).

31. Xie, Y. *et al.* Fractional Chern insulators in magic-angle twisted bilayer graphene. *arXiv: 2107.10854* (2021).
32. Hunt, B. *et al.* Massive Dirac Fermions and Hofstadter Butterfly in a van der Waals Heterostructure. *Science* **340**, 1427–1430 (2013).
33. Saito, Y. *et al.* Hofstadter subband ferromagnetism and symmetry-broken Chern insulators in twisted bilayer graphene. *Nat. Phys.* **17**, 478–481 (2021).

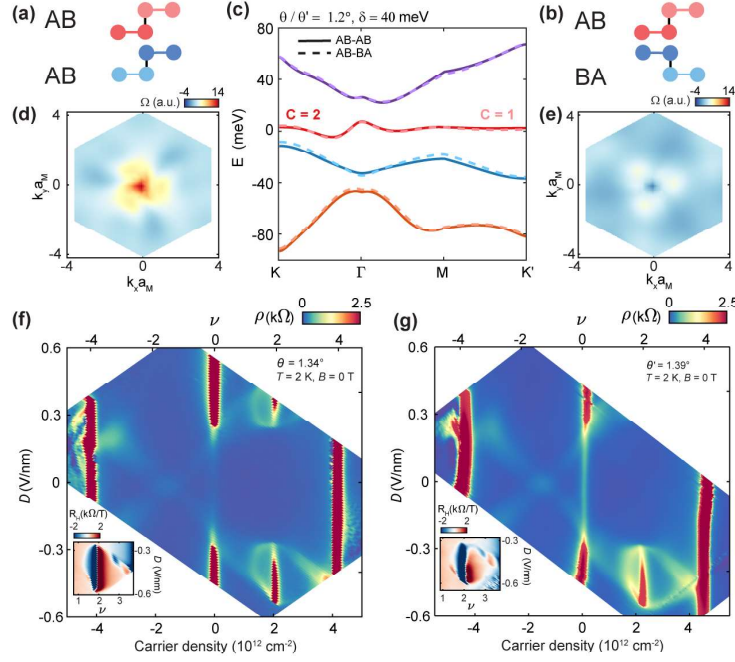


**Figure 1. Chirality dependent stacking arrangement in twisted double bilayer graphene (tDBG) .** **a-b**, Side-view lattice schematics of AB-AB and AB-BA tDBG. AB-AB (AB-BA) tDBG is composed of two Bernal stacked graphene bilayers with the same (opposite) stacking chirality. **c**, Calculated band structure of  $\theta = 1.2^\circ$  (AB-AB, solid line) and  $\theta' = 1.2^\circ$  (AB-BA, dashed line) tDBG, with interlayer potential  $\delta = 40$  meV. The red bands denote the lowest moiré conduction band, whose the Chern number in AB-AB (AB-BA) tDBG is  $C = 2$  (1). **d-e**, Corresponding Berry curvature ( $\Omega$ ) of the lowest moiré conduction band for AB-AB and AB-BA, respectively, with  $\delta = 40$  meV.  $k$  is in units of  $1/a_M$ , where  $a_M$  is the moiré lattice constant. **f-g**, Resistivity  $\rho_{xx}$  maps of  $\theta = 1.34^\circ$  (AB-AB) and  $\theta' = 1.39^\circ$  (AB-BA) tDBG devices, respectively. Measurements are taken at  $T = 2$  K with zero magnetic field. Insets shows the zoomed-in Hall coefficient  $R_H$  at  $|B| = 0.5$  T, focusing on the correlated phases.

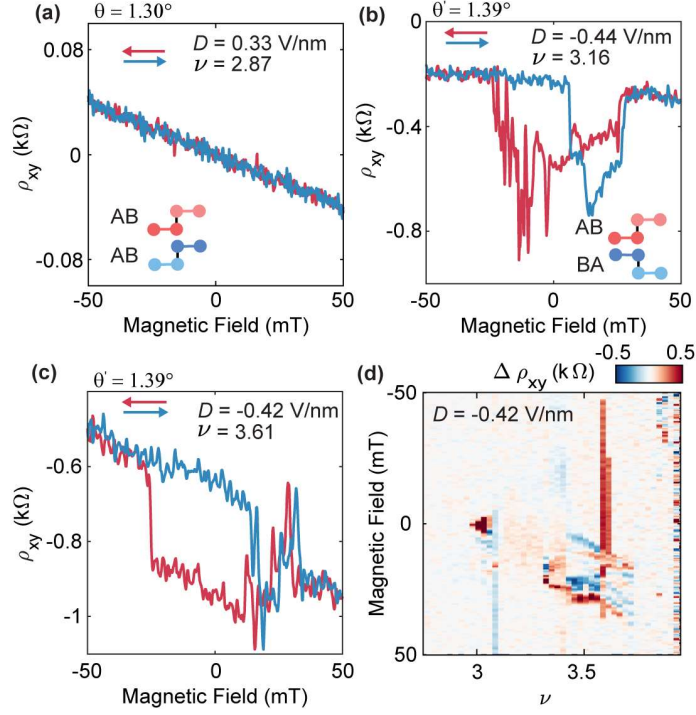


**Figure 2. Anomalous Hall effect near integer filling  $\nu = 3$  and fractional filling  $\nu = 7/2$ .** **a**,  $\rho_{xy}$  measured as magnetic field is swept back and forth at  $\nu = 2.87$ ,  $D = 0.33$  V/nm in AB-AB tDBG with  $\theta = 1.30^\circ$ . **b**, Similar measurements at  $\nu = 3.16$ ,  $D = -0.44$  V/nm in AB-BA tDBG with  $\theta' = 1.39^\circ$ . AHE is observed only in the AB-BA sample. **c**, Similar measurements in the AB-BA sample at  $\nu = 3.61$ ,  $D = -0.42$  V/nm. **d**,  $\Delta\rho_{xy} = \rho_{xy}^{B\downarrow} - \rho_{xy}^{B\uparrow}$  plotted as a function of magnetic field measured over a range of filling factors at fixed  $D = -0.42$  V/nm.  $T = 100$  mK for all measurements.

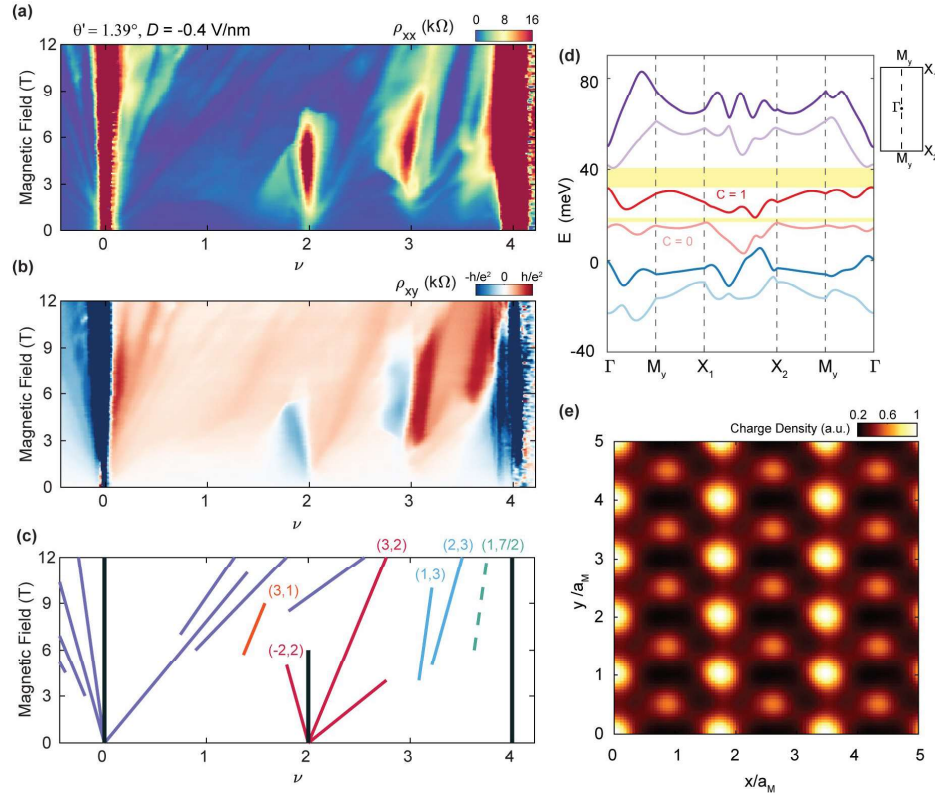


**Figure 3.  $C = 1$  symmetry broken Chern insulator at  $\nu = 7/2$ .** **a-b**, Landau fan diagram of the longitudinal ( $\rho_{xx}$ ) and Hall ( $\rho_{xy}$ ) resistivity at  $D = -0.4$  V/nm. Data is taken at 100 mK. **c**, Schematics of all observed gapped states in **a-b**. Several main gapped states are labelled by their respective  $(C, s)$  values. Colors differentiate different values of  $s$ . Black vertical lines (with  $C = 0$ ) denote topologically trivial insulating states. The green dashed line denotes the SBCI state  $(1, 7/2)$ . **d**, Calculated band structure reconstructed with charge density wave order ( $\Phi = 16$  meV). The red bands are the two split subbands from the lowest moiré conduction band with a CDW gap of  $\Delta = 2$  meV. Chern numbers are labeled for the two conduction subbands. **e**, Calculated density profile in real space after introducing the CDW order. A gauge is chosen to pin the maximum of the CDW order to the AA sites.  $a_M$  is the moiré lattice constant.

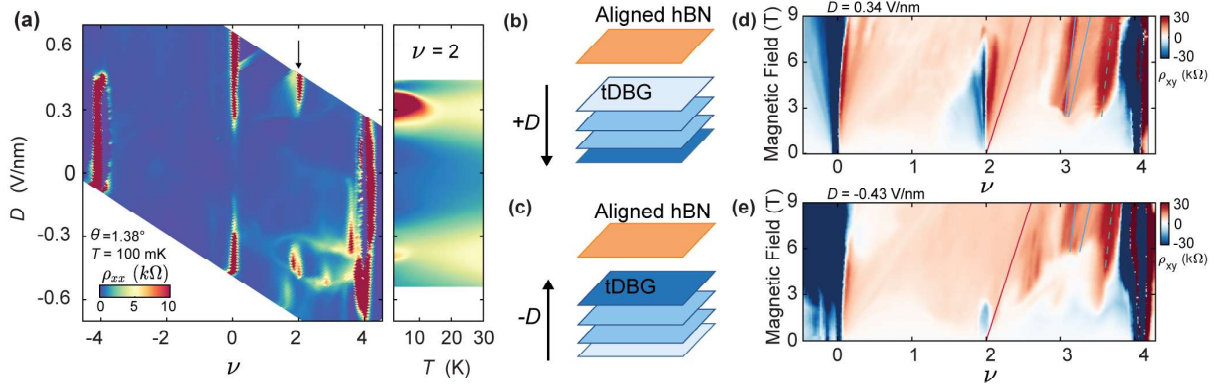


**Figure 4. Robust SBCI with additional top hBN alignment.** **a**, Resistivity ( $\rho_{xx}$ ) map of a  $\theta' = 1.38^\circ$  AB-BA tDBG device aligned with top hBN at a twist angle of  $0.55^\circ$ . The right panel shows  $\rho_{xx}$  as function of temperature and  $D$  at  $\nu = 2$ . **b-c**, Schematics of the layer-resolved electron density upon a positive and negative  $D$ , respectively. The electron density is schematically indicated by intensity of blue coloring. **d-e**, Hall resistivity,  $\rho_{xy}$ , measured at  $D = 0.34$  V/nm (top) and  $D = -0.43$  V/nm (bottom), respectively. Schematics of observed gapped states are overlayed, using the same color coding as in Fig. 3.

**Supplementary Information for:**  
**Chirality-dependent topological states in twisted double bilayer graphene**

Minhao He<sup>1†</sup>, Jiaqi Cai<sup>1†</sup>, Ya-Hui Zhang<sup>2</sup>, Yang Liu<sup>1</sup>, Yuhao Li<sup>1</sup>, Takashi Taniguchi<sup>3</sup>,  
Kenji Watanabe<sup>4</sup>, David H. Cobden<sup>1</sup>, Matthew Yankowitz<sup>1,5‡</sup>, and Xiaodong Xu<sup>1,5‡</sup>

<sup>1</sup>*Department of Physics, University of Washington, Seattle, Washington, 98195, USA*

<sup>2</sup>*Department of Physics, Harvard University, Cambridge, MA, USA*

<sup>3</sup>*International Center for Materials Nanoarchitectonics,*

*National Institute for Materials Science, 1-1 Namiki, Tsukuba 305-0044, Japan*

<sup>4</sup>*Research Center for Functional Materials, National Institute for Materials Science, 1-1 Namiki, Tsukuba 305-0044, Japan*

<sup>5</sup>*Department of Materials Science and Engineering,*

*University of Washington, Seattle, Washington, 98195, USA*

<sup>†</sup> *These authors contributed equally to the work. and*

<sup>‡</sup> *myank@uw.edu (M.Y.); xuxd@uw.edu (X.X.)*

### Supplementary Note 1. Band structure calculation of AB-BA tDBG

We calculate the band structure of the AB-BA stacked tDBG based on the standard Bistritzer MacDonald continuum model. The full Hamiltonian for the valley  $K$  is:

$$H = H_t^{AB} + H_b^{BA} + H_M \quad (1)$$

where  $H_t^{AB}$  and  $H_b^{BA}$  are the Hamiltonian of the two layers separately.  $H_M$  includes the interlayer moiré tunneling terms. We have

$$H_t^{AB} = \Psi_t^\dagger \begin{pmatrix} \frac{D}{2} & t(k_x - ik_y)e^{i\frac{\theta}{2}} & t_4(k_x - ik_y)e^{i\frac{\theta}{2}} & t_3(k_x + ik_y)e^{-i\frac{\theta}{2}} \\ t(k_x + ik_y)e^{-i\frac{\theta}{2}} & \frac{D}{2} & \gamma_1 & t_4(k_x - ik_y)e^{i\frac{\theta}{2}} \\ t_4(k_x + ik_y)e^{-i\frac{\theta}{2}} & \gamma_1 & \frac{D}{6} & t(k_x - ik_y)e^{i\frac{\theta}{2}} \\ t_3(k_x - ik_y)e^{i\frac{\theta}{2}} & t_4(k_x + ik_y)e^{-i\frac{\theta}{2}} & t(k_x + ik_y)e^{-i\frac{\theta}{2}} & \frac{D}{6} \end{pmatrix} \Psi_t \quad (2)$$

and

$$H_b^{BA} = \Psi_b^\dagger \begin{pmatrix} -\frac{D}{6} & t(k_x - ik_y)e^{-i\frac{\theta}{2}} & t_4(k_x + ik_y)e^{i\frac{\theta}{2}} & \gamma_1 \\ t(k_x + ik_y)e^{i\frac{\theta}{2}} & -\frac{D}{6} & t_3(k_x - ik_y)e^{-i\frac{\theta}{2}} & t_4(k_x + ik_y)e^{i\frac{\theta}{2}} \\ t_4(k_x - ik_y)e^{-i\frac{\theta}{2}} & t_3(k_x + ik_y)e^{i\frac{\theta}{2}} & -\frac{D}{2} & t(k_x - ik_y)e^{-i\frac{\theta}{2}} \\ \gamma_1 & t_4(k_x - ik_y)e^{-i\frac{\theta}{2}} & t(k_x + ik_y)e^{i\frac{\theta}{2}} & -\frac{D}{2} \end{pmatrix} \Psi_b \quad (3)$$

In the above, we choose basis as  $\Psi_{t/b} = (f_{A_{t/b;1}}, f_{A_{t/b;2}}, f_{B_{t/b;1}}, f_{B_{t/b;2}})^T$  and  $f_{A_{t/b;1}}, f_{A_{t/b;2}}, f_{B_{t/b;1}}, f_{B_{t/b;2}}$  label the layer-sublattice degree of freedom of the top/bottom bilayer graphene. We use the parameters  $t = -3100\frac{\sqrt{3}}{2}$  meV,  $t_1 = 283\frac{\sqrt{3}}{2}$  meV,  $t_4 = 110\frac{\sqrt{3}}{2}$  meV and  $\gamma_1 = 361$  meV, where the momentum  $k_x, k_y$  is in the unit of  $\frac{1}{a}$ , and  $a \approx 0.246$  nm is the lattice constant of graphene.

The interlayer moiré tunneling Hamiltonian  $H_M$  is

$$H_M = \sum_{j=1,2,3} (f_{A_{t;2}}^\dagger(\mathbf{k}), f_{B_{t;2}}^\dagger(\mathbf{k})) T_j \begin{pmatrix} f_{A_{b;1}}(\mathbf{k} + \mathbf{Q}_j) \\ f_{B_{b;1}}(\mathbf{k} + \mathbf{Q}_j) \end{pmatrix} + h.c. \quad (4)$$

where  $\mathbf{Q}_1 = 0$ ,  $\mathbf{Q}_2 = \mathbf{G}_1 = (-\frac{2\pi}{\sqrt{3}a_M}, -\frac{2\pi}{a_M})$ , and  $\mathbf{Q}_3 = \mathbf{G}_2 = (\frac{2\pi}{\sqrt{3}a_M}, -\frac{2\pi}{a_M})$ . The moiré lattice constant at twist angle  $\theta$  is denoted as  $a_M = \frac{a}{2\sin\frac{\theta}{2}}$ . We have  $T_j = t_M \begin{pmatrix} \alpha & e^{-i\frac{2\pi j}{3}} \\ e^{i\frac{2\pi j}{3}} & \alpha \end{pmatrix}$ , where  $t_M$  is the interlayer tunneling strength and  $\alpha \in [0, 1]$  is introduced to incorporate the effects of lattice relaxation. We use  $t_M = 110$  meV and  $\alpha = 0.8$ .

At the limit of  $D = 0$ , there is a mirror symmetry  $M : k_x \rightarrow k_x, k_y \rightarrow -k_y$ , which acts as  $M_y K$ , where  $K$  is the complex conjugate.  $M_y$  maps  $A_{t;1} \rightarrow A_{b;2}, A_{t;2} \rightarrow A_{b;1}, B_{t;1} \rightarrow B_{t;2}, B_{t;2} \rightarrow B_{b;2}$ , where the momentum changes as  $k_x \rightarrow -k_x, k_y \rightarrow k_y$ . There is no flip of the valley index in this transformation. We note that the realization of the mirror symmetry is different for the AB-AB stacked tDBG, in which  $M : k_x \rightarrow k_x, k_y \rightarrow -k_y$ , acting as  $M_x$ , with  $A_{t;1} \rightarrow B_{b;2}, A_{t;2} \rightarrow B_{b;1}, B_{t;1} \rightarrow A_{b;2}, B_{t;2} \rightarrow A_{t;2}$ . Again there is no valley flip in the transformation. Note that there is no complex conjugate compared to the AB-BA stacking. As a result, the constraint of the Chern number  $C$  is different. For AB-AB stacking, we have  $C(D) = -C(-D)$  within one valley, while we have  $C(D) = C(-D)$  within each valley for the AB-BA stacking.

### Supplementary Note 2. Comparison of band dispersion and its topology

The band dispersions of AB-AB tDBG and AB-BA tDBG are quite similar [1–5]. We calculate the band structure of tDBG in both stacking chiralities at  $\theta(\theta') = 1.2^\circ$  with a finite  $D$ , represented by interlayer potential  $\delta = 40$  meV. Although the band structures are almost identical (Fig. 1c of the main text), the Berry curvature distributions are

very different, as shown in Figs. 1d-e of the main text. For AB-AB stacked tDBG, the Berry curvature from the K and K' points of the moiré Brillouin zone are the same and sum together to result in  $C = 2$  for the lowest conduction band. In contrast, for AB-BA tDBG,  $K$  and  $K'$  carry opposite Berry curvatures. The net Berry curvature comes primarily from the center region of the moiré Brillouin zone (*i.e.*, the  $\Gamma$  point), resulting in  $C = 1$ .

### Supplementary Note 3. Topological charge density wave

We calculate reconstructed band structure and Chern number at  $\nu = \frac{1}{2}$  after adding a phenomenological CDW order with  $2 \times 1$  Moiré unit cell in the AB-BA stacked tDBG.

The CDW is generated by a potential with nesting momentum  $\mathbf{Q} = (\frac{2\pi}{\sqrt{3}a_M}, 0)$ . The interaction Hamiltonian at this momentum is given as:

$$H_V = V(\mathbf{Q})\rho(\mathbf{Q})\rho(-\mathbf{Q}) \quad (5)$$

where  $\rho(\mathbf{Q})$  is the density operator projected to the active band and  $V(\mathbf{Q})$  is the Fourier-transformed screened Coulomb potential.

The mean field Hamiltonian decoupled from the interaction is:

$$H = H_{\text{nonint}} + (\Phi\rho(\mathbf{Q}) + h.c.) \quad (6)$$

where,  $H_{\text{nonint}}$  is non-interacting Hamiltonian defined in Eq.1,  $\Phi = V(\mathbf{Q})\langle\rho(\mathbf{Q})\rangle$  is the charge density wave order parameter. In a more detailed form:

$$H = H_{\text{nonint}} + \sum_{\mathbf{k}} (\Phi\Lambda_{ab}(\mathbf{k}, \mathbf{Q}) + \Phi^*\Lambda_{ab}(\mathbf{k}, -\mathbf{Q}))c_a^\dagger(\mathbf{k} + \mathbf{Q})c_b(\mathbf{k}) + h.c. \quad (7)$$

where  $\Lambda_{ab}(\mathbf{k}, \mathbf{q}) = \langle\mu_a(\mathbf{k} + \mathbf{q})|\mu_b(\mathbf{k})\rangle$  is a form-factor entering the density operator.  $\mu_a(\mathbf{k})$  is the Bloch wavefunction for band  $a$ .

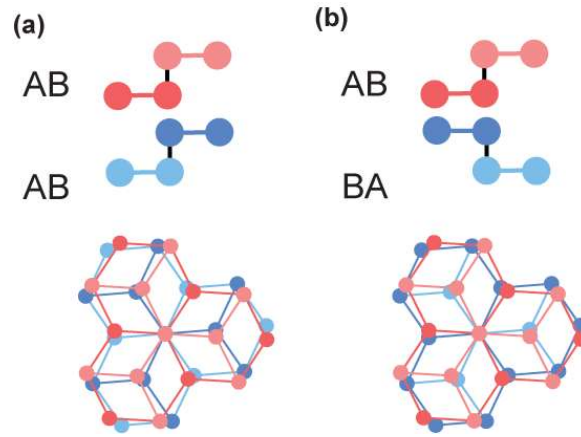
Note here  $\Phi$  can be a complex number, whose phase  $\phi$  determines the phase of the CDW order  $\rho(\mathbf{r}) = \rho_0 + A\cos(\pi x + \phi)$ , where  $x$  is the coordinate along the  $\mathbf{a}_1$  direction. We label the AA site (maximum of the LDOS) as  $\mathbf{r} = 0$  and choose  $\phi = 0$  to pin the CDW with the moiré lattice (see Fig. 3e of the main text).

In the original electron operator,

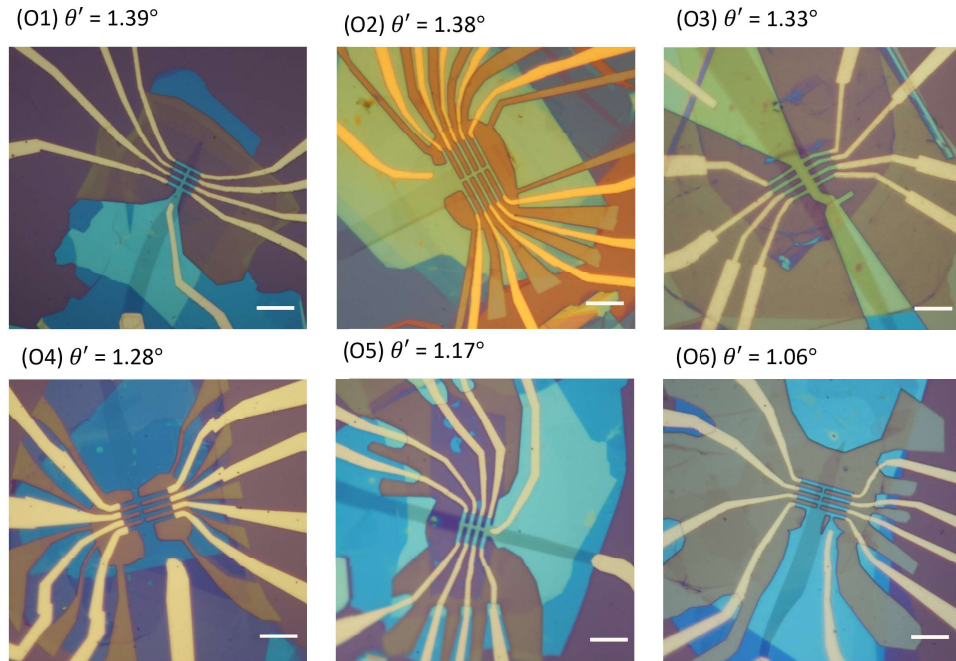
$$H = H_{\text{nonint}} + \sum_{\mathbf{k}} \sum_{a,b} (\Phi\Lambda_{ab}(\mathbf{k}, \mathbf{Q}) + \Phi^*\Lambda_{ab}(\mathbf{k}, -\mathbf{Q}))\mu_{a;\alpha}(\mathbf{k} + \mathbf{Q})\mu_{b;\beta}^*(\mathbf{k})f_\alpha^\dagger(\mathbf{k} + \mathbf{Q})f_\beta(\mathbf{k}) + h.c. \quad (8)$$

where  $\alpha, \beta$  is a combination of the sublattice-layer index and the  $m\mathbf{G}_1 + n\mathbf{G}_2$  index.  $a, b$  is the band index. We sum  $a, b$  with  $M$  to be the band index cutoff, *i.e.*, over the conduction band,  $M$  bands below and  $M$  bands above. If we set  $M = 0$ , then the CDW only influences the conduction band. If  $M \geq 1$ , the CDW order also acts on the remote bands and couples the remote band to the conduction band. In practice, the result converges quite rapidly when increasing  $M$ . However, we note that  $M \geq 1$  and  $M = 0$  can give different results. The CDW order also hybridizes the remote band and the conduction band, which can renormalize the Chern number of the upper band split from the remainder of the conduction band.

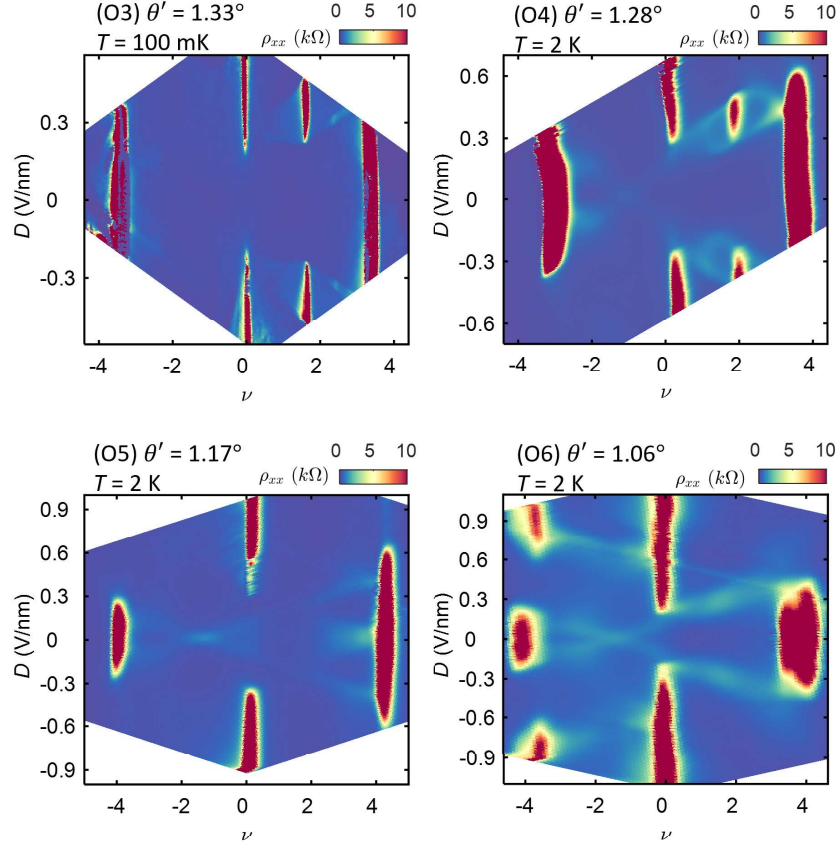
We consider tDBG in both stacking chiralities at the same condition discussed above. In AB-AB tDBG, it is natural to expect that a CDW with  $2 \times 1$  unit cell will split the original  $C = 2$  conduction band into two  $C = 1$  and  $C = 1$  subbands. However, for AB-BA stacking, the  $C = 1$  conduction band will split into a  $C = 0$  and  $C = 1$  band: the half around the zone center region carries  $C = 1$ , whereas the half around the  $K$  and  $K'$  carries  $C = 0$ . We calculate band structure in AB-BA tDBG with a CDW order  $\Phi = 16$  meV in Supplementary Fig. 9. We find that the Chern numbers of the gapped subbands are sensitive to the remote band renormalization. For  $M = 0$ , the upper subband has  $C = 0$ , inconsistent with our experimental observations of a topological state at  $\nu = \frac{7}{2}$ . After considering  $M = 4$  remote bands, the Chern number of the upper subband renormalizes to  $C = 1$ , in agreement with our experiment. We note that  $M = \infty$  (*i.e.* the realistic limit) should yield the same result for the conduction band as  $M = 4$  in our calculation owing to its rapid convergence.



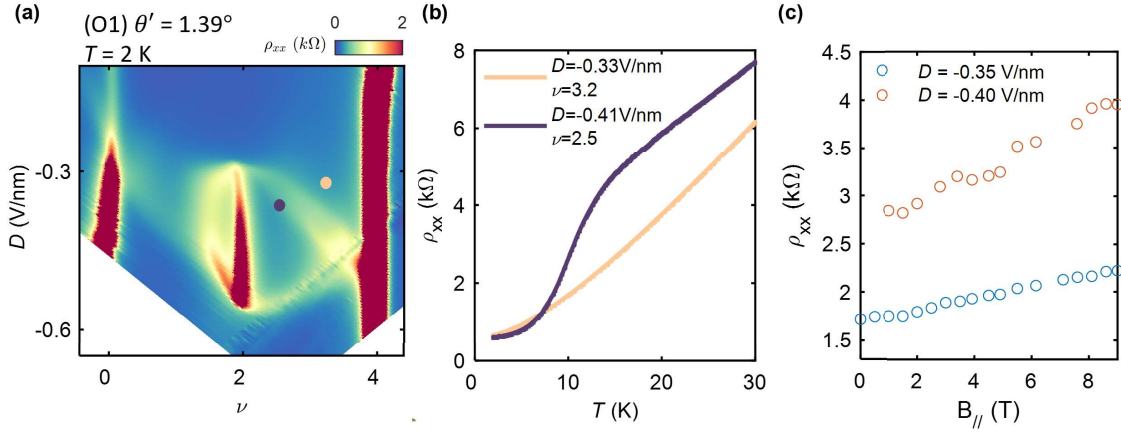
Supplementary Figure 1. **Schematic drawings of AB-AB and AB-BA tDBG.** a-b, Lattice schematics of AB-AB and AB-BA tDBG, respectively. The component Bernal graphene bilayers are rotated near  $0^\circ$  and  $60^\circ$  in the two cases. The top row shows the side view while the bottom row shows the top view, focusing on the high symmetry local registry.



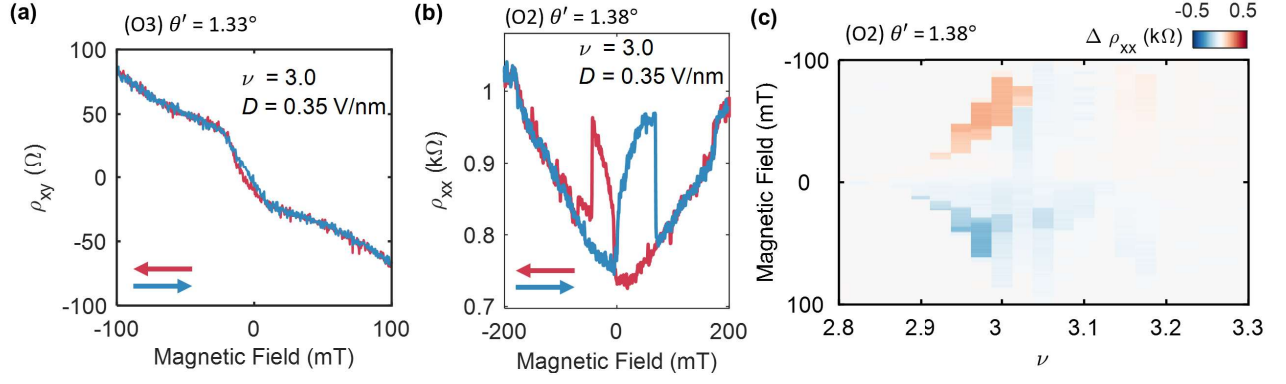
Supplementary Figure 2. **Optical images of the AB-BA tDBG devices.** Twist angles are denoted at the top left corner of each image. All scale bars are  $10 \mu\text{m}$ .



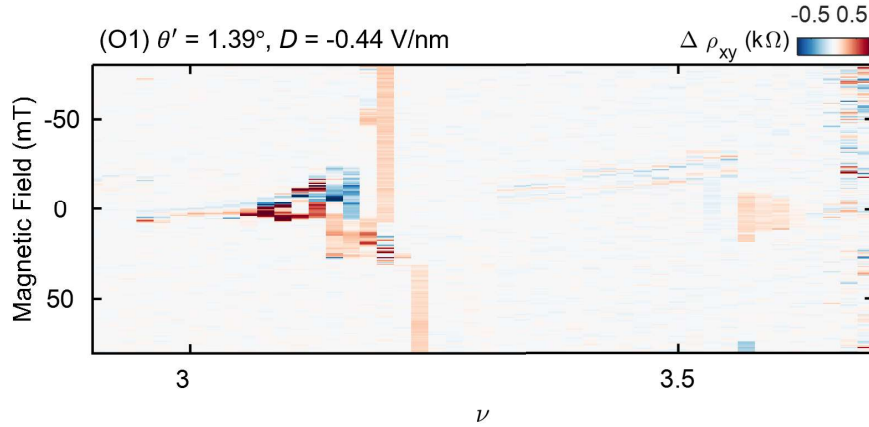
Supplementary Figure 3. **Low temperature transport in additional AB-BA tDBG devices.** The twist angle and measurement temperature are denoted at the top left corner of each map. We observe displacement field-tunable insulating states at  $\nu = 0$  and  $\pm 4$  in all devices. Correlated insulating states appear clearly in devices O3 and O4.



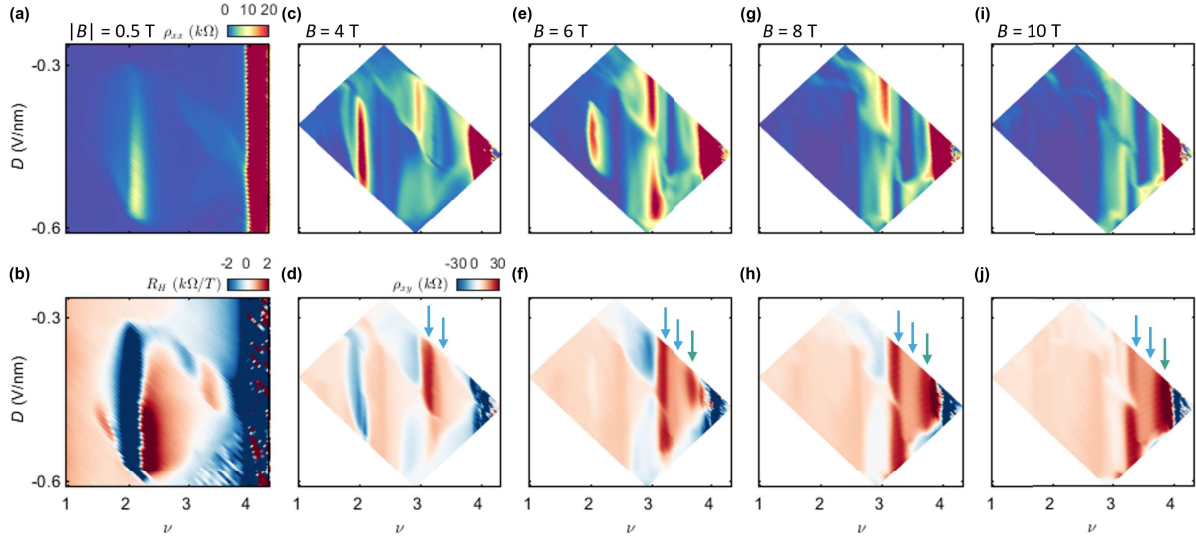
Supplementary Figure 4. **Correlated phases in a  $\theta' = 1.39^\circ$  AB-BA tDBG device (O1).** **a**,  $\rho_{xx}$  map of device O1 at  $T = 2$  K. **b**,  $\rho_{xx}$  as a function of temperature inside (purple) and outside (yellow) the symmetry-broken metallic regime.  $\rho_{xx}$  drops abruptly with temperature inside the symmetry-broken regime (purple curve), similar to observations in AB-AB tDBG [6–10]. This behavior is not observed outside the ‘halo’-like region (orange curve). **c**,  $\rho_{xx}$  as a function of in-plane magnetic field,  $B_{||}$ , at the  $\nu = 2$  correlated insulating state with different  $D$ . We observe a weak increase of  $\rho_{xx}$ , suggesting that it may be spin-polarized as in AB-AB tDBG [6–10].



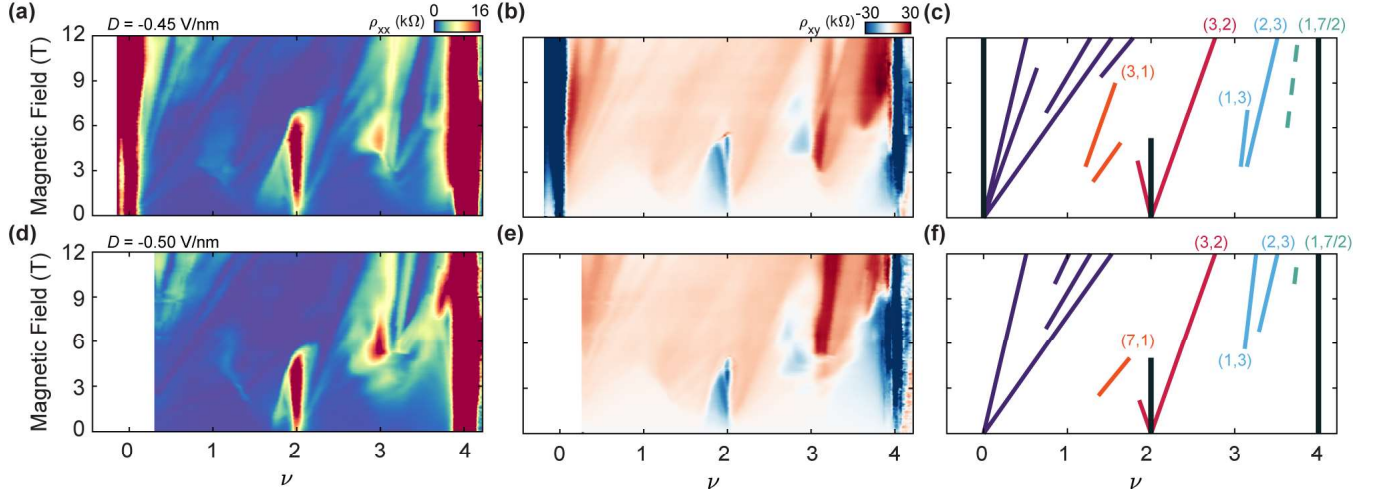
Supplementary Figure 5. **AHE near  $\nu = 3$  in other AB-BA tDBG devices.** **a**, Hall ( $\rho_{xy}$ ) resistivity as the magnetic field is swept back and forth at specified  $\nu$ ,  $D$  in the  $\theta' = 1.33^\circ$  device. Data is acquired at base temperature of 50 mK.  $\rho_{xy}$  shows kink in the slope and a small hysteric loop at zero field. This suggests emerging AHE at  $\nu = 3$ . **b**,  $\rho_{xx}$  as field swept back and forth at specified  $\nu$ ,  $D$  in the  $\theta' = 1.38^\circ$  device. **c**,  $\Delta\rho_{xx}$  as a function of magnetic field measured at different filling factor with fixed  $D = 0.35$  V/nm in the same device. **c,d**, data are acquired at 300 mK. The device does not have a proper contact pair to measure  $\rho_{xy}$  of the magnetic region. Nevertheless, the observed hysteresis in  $\rho_{xx}$  indicates the AHE at  $\nu = 3$ .



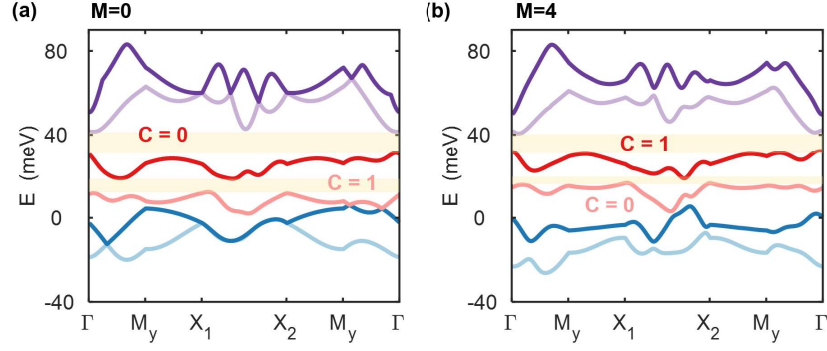
Supplementary Figure 6. **Isolated AHE near  $\nu = 3$  and  $\nu = 7/2$ .**  $\Delta\rho_{xy}$  as a function of magnetic field measured at different filling factor at fixed  $D = -0.44$  V/nm in the  $\theta' = 1.39^\circ$  AB-BA tDBG device (O1). We define  $\Delta\rho_{xy} = \rho_{xy}^{B\downarrow} - \rho_{xy}^{B\uparrow}$  to visualize the AHE. The AHE at  $\nu = 3$  and  $\nu = 7/2$  are isolated, indicating they are likely independent correlated states. Data is acquired at 100 mK.



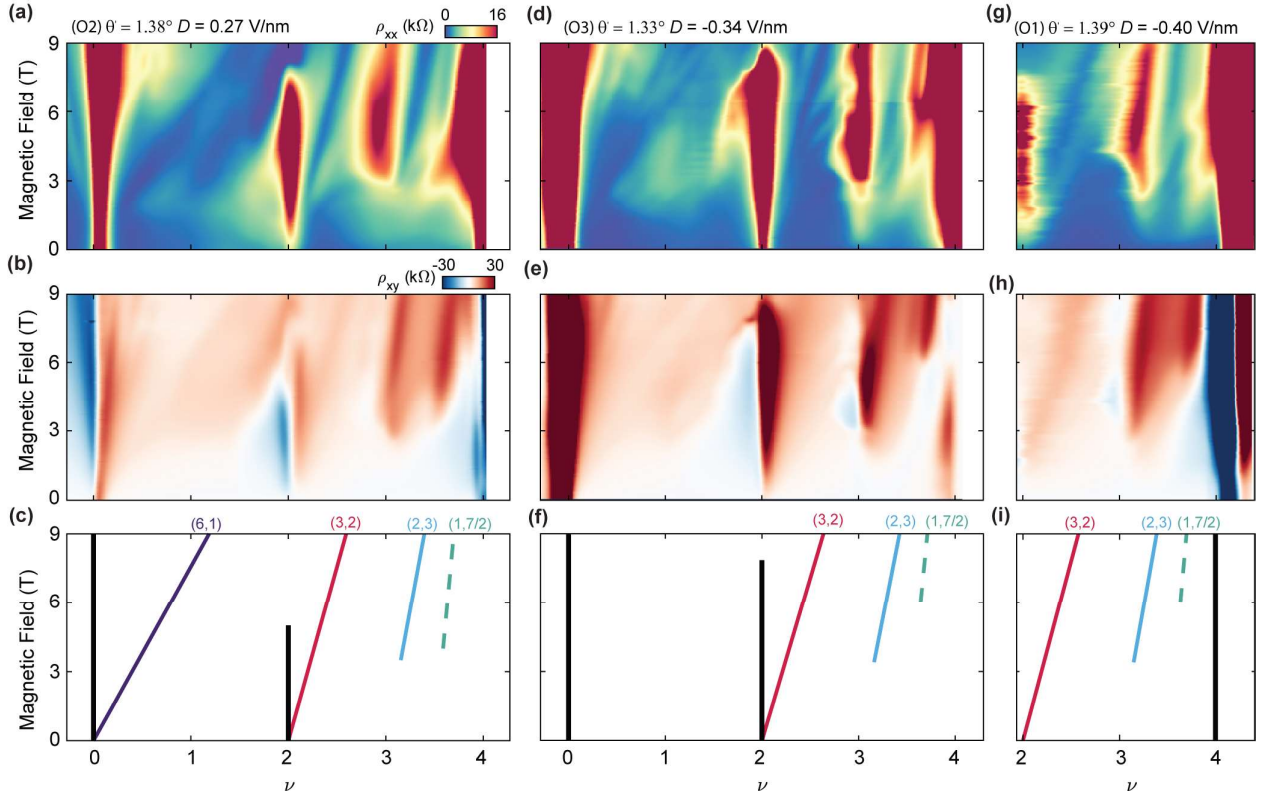
Supplementary Figure 7. **Evolution of Chern insulators and the  $(1, 7/2)$  SBCI with magnetic field in the  $\theta' = 1.39^\circ$  AB-BA tDBG device (O1).** a-b, Resistivity  $\rho_{xx}$  and Hall coefficient  $R_H$  map as a function of  $D$  and  $\nu$ , acquired at  $|B| = 0.5$  T.  $\rho_{xx}$  and  $R_H$  are field symmetrized and anti-symmetrized, respectively. c-j,  $\rho_{xx}$  and  $\rho_{xy}$  map at  $B = 4, 6, 8$ , and  $10$  T, respectively. Blue arrows denotes Chern insulators associated with  $s = 3$ . The green arrow denotes the  $(1, 7/2)$  SBCI, which emerges above  $6$  T. All data are acquired at  $100$  mK.



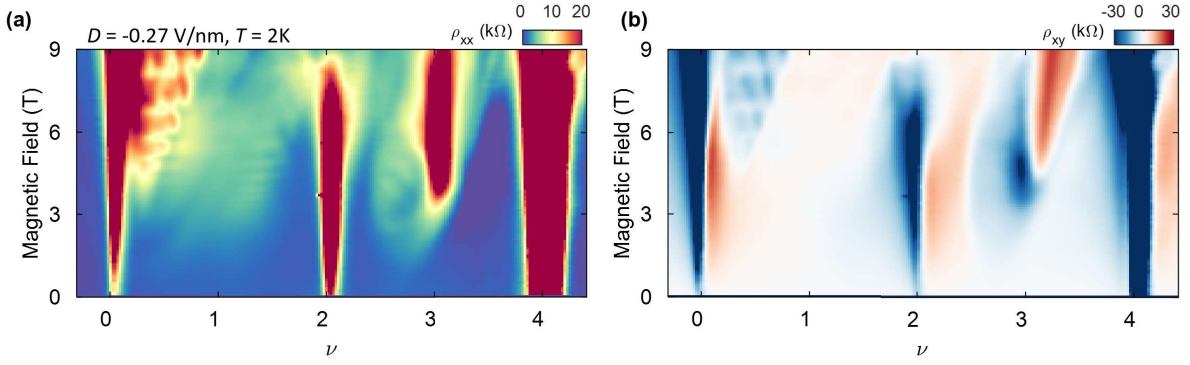
Supplementary Figure 8. **Landau fan diagrams in the  $\theta' = 1.39^\circ$  AB-BA tDBG device (O1) at selected  $D$ .** The left column shows the longitudinal resistivity ( $\rho_{xx}$ ), the middle shows the Hall resistivity ( $\rho_{xy}$ ), and right shows corresponding schematics of observed gapped states.  $D = -0.45$  V/nm for a-c, and  $D = -0.50$  V/nm for d-f. c,f, use the same color scheme as in Fig. 3c of the main text. All data are acquired at  $100$  mK.



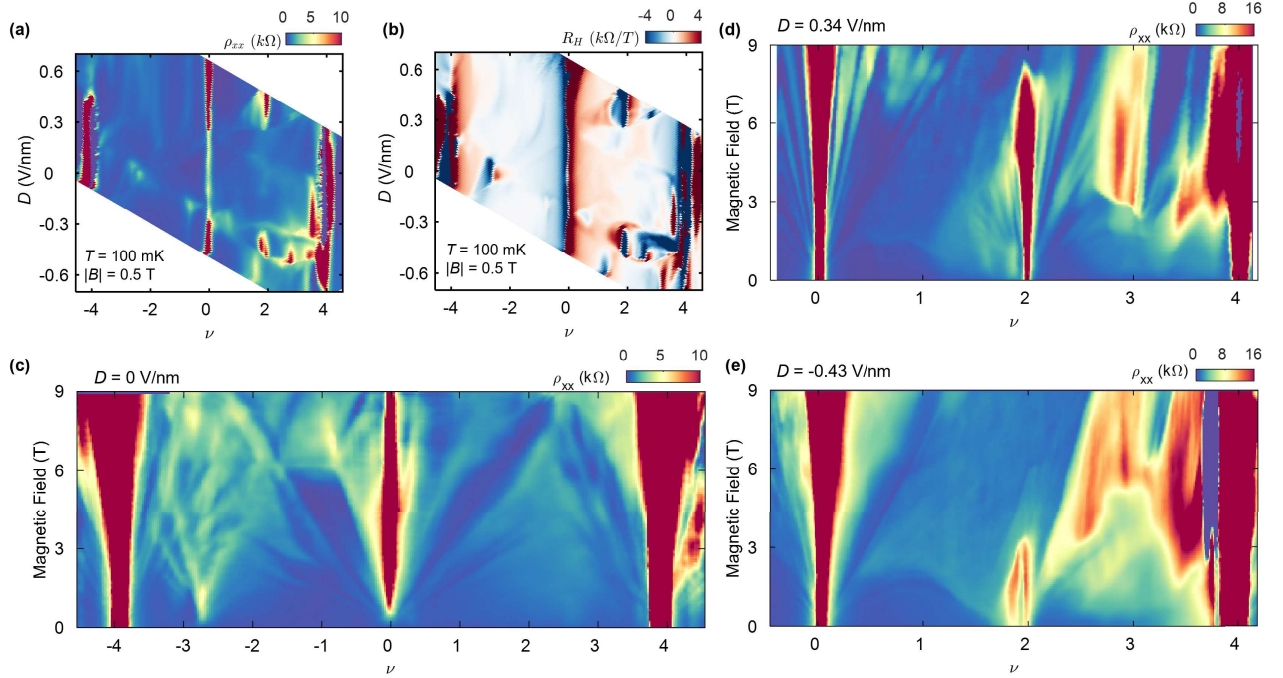
Supplementary Figure 9. **Reconstructed band structure with CDW order.** Calculated band structure of AB-BA tDBG at  $\theta' = 1.2^\circ$ ,  $\delta = 40$  meV, with charge density wave order  $\Phi = 16$  meV. The red and blue bands denote the gapped subbands of the lowest moiré conduction and valence bands, respectively. The red subbands are split with a CDW gap of  $\Delta = 2$  meV. The associated Chern numbers are labeled just above each conduction subband. We consider remote band renormalization with cutoff  $M$ , denoting number of remote bands considered. Results with  $M = 0$  and  $M = 4$  shown in **a,b** respectively. The partitioning of the Chern number of the conduction band is sensitive to  $M$ , and quickly converges when  $M > 1$  to its real value (i.e., the value at  $M = \infty$ ).



Supplementary Figure 10. **Robust SBCI at  $T = 2$  K observed in additional AB-BA tDBG devices.** Landau fan diagram in resistivity  $\rho_{xx}$ , Hall resistivity  $\rho_{xy}$  and schematic of the observed gapped states for device (O2)  $\theta' = 1.38^\circ$  device in **a-c**, device (O3)  $\theta' = 1.33^\circ$  in **d-f**, and device (O1)  $\theta' = 1.39^\circ$  device in **g-i**. **c,f,i** use the same color scheme as in Fig. 3c of the main text. All data are acquired at  $T = 2$  K. We find that the  $(1, 7/2)$  SBCI state as a robust ground state in AB-BA tDBG, and persists up to at least 2 K in all three devices shown.



Supplementary Figure 11. **Absence of the  $(1, 7/2)$  SBCI in AB-AB tDBG.** a-b, Landau fan in resistivity  $\rho_{xx}$  and Hall resistivity  $\rho_{xy}$  measured at  $D = -0.27$  V/nm in a  $\theta = 1.30^\circ$  AB-AB tDBG (device S2), measured at  $T = 2$  K. We do not observe a SBCI state in this AB-AB tDBG device, nor any of the others we have measured, nor has it been reported in previous studies [6–9].



Supplementary Figure 12.  $\theta' = 1.38^\circ$  AB-BA tDBG device aligned with hBN. a,b, Resistivity  $\rho_{xx}$  and Hall coefficient  $R_H$  map, field symmetrized and anti-symmetrized with  $|B| = 0.5$  T, respectively. c, Landau fan diagram of the longitudinal resistivity  $\rho_{xx}$  at  $D = 0$  V/nm. Additional set of gapped states are seen emerging from  $\nu \approx -2.8$ , corresponding to the secondary Dirac point from the graphene/hBN moiré. We calculate the twist angle between graphene and hBN to be  $0.55^\circ$  based on the carrier density of the secondary Dirac point. d,e, Landau fan of  $\rho_{xx}$  at  $D = +0.34$  V/nm and  $D = -0.43$  V/nm, respectively. The gapped states observed in the Landau fans vary substantially with the sign of  $D$  owing to the alignment of the hBN on one side. All data are acquired at 100 mK.

## REFERENCES

- [1] Zhang, Y.-A., Mao, D., Cao, Y., Jarillo-Herrero, P. & Senthil, T. Nearly flat chern bands in moiré superlattices. *Physical Review B* **99**, 075127 (2019).
- [2] Lee, J. Y. *et al.* Theory of correlated insulating behaviour and spin-triplet superconductivity in twisted double bilayer graphene. *Nature Communications* **10**, 5333 (2019).
- [3] Chebrolu, N. R., Chittari, B. L. & Jung, J. Flat bands in twisted double bilayer graphene. *Physical Review B* **99**, 235417 (2019).
- [4] Liu, J., Ma, Z., Gao, J. & Dai, X. Quantum valley hall effect, orbital magnetism, and anomalous hall effect in twisted multilayer graphene systems. *Physical Review X* **9**, 031021 (2019).
- [5] Koshino, M. Band structure and topological properties of twisted double bilayer graphene. *Physical Review B* **99**, 235406 (2019).
- [6] Burg, G. W. *et al.* Correlated insulating states in twisted double bilayer graphene. *Physical Review Letters* **123**, 197702 (2019).
- [7] Liu, X. *et al.* Tunable spin-polarized correlated states in twisted double bilayer graphene. *Nature* 221–225 (2019).
- [8] Cao, Y. *et al.* Tunable correlated states and spin-polarized phases in twisted bilayer–bilayer graphene. *Nature* 215–220 (2020).
- [9] Shen, C. *et al.* Correlated states in twisted double bilayer graphene. *Nature Physics* **16**, 520–525 (2020).
- [10] He, M. *et al.* Symmetry breaking in twisted double bilayer graphene. *Nature Physics* **17**, 26–30 (2021).